Supplementary file

Maturity-controlled competitive adsorption of CO_2-H_2 and CH_4-H_2 mixtures in shale kerogen nanopores

Zhikai Liang[1,2], Zhenxue Jiang[3*], Mehdi Ostadhassan[4], Guangyou Zhu[1,2], Zhuo Li[3], Muhammad Arif[5*]

[1]*Key Laboratory of Exploration Technologies for Oil and Gas Resources, Ministry of Education, Yangtze University, Wuhan 430100, P. R. China*

[2]*School of Geosciences, Yangtze University, Wuhan 430100, P. R. China*

[3]*State Key Laboratory of Petroleum Resources and Engineering, China University of Petroleum, Beijing 102249, P. R. China*

[4]*Institute of Geosciences, Marine and Land Geomechanics and Geotectonics, Christian-Albrechts-Universitat, Kiel 24118, Germany*

[5]*Department of Chemical & Petroleum Engineering, Khalifa University, Abu Dhabi 127788, United Arab Emirates*

E-mail address: liangzhikai2020@163.com (Z. Liang); jiangzx@cup.edu.cn (Z. Jiang); mehdi.ostadhassan@ifg.uni-kiel.de (M. Ostadhassan); zhuguangyou@yangtzeu.edu.cn (G. Zhu); zhuo.li@cup.edu.cn (Z. Li); muhammad.arif@ku.ac.ae (Arif. M).

[*]Corresponding author (ORCID: 0000-0002-2553-4573 (Z. Jiang); 0000-0001-7035-6000 (Arif. M))

Liang, Z., Jiang, Z., Ostadhassan, M., Zhu, G., Li, Z., Arif, M. Maturity-controlled competitive adsorption of CO_2-H_2 and CH_4-H_2 mixtures in shale kerogen nanopores. Advances in Geo-Energy Research, 2026, 20(3): 259-276.

The link to this file is: https://doi.org/10.46690/ager.2026.06.07

Appendix A: Analytical methods

Section 1

(1) Detailed procedure for kerogen molecular model construction

The molecular structures of the high-maturity and overmature kerogen models were constructed based on experimental constraints from elemental analysis, XPS, FTIR, and solid-state ^{13}C NMR. The general construction strategy followed previously reported kerogen reconstruction workflows, while the structural parameters were adjusted according to the experimental results obtained in this study.

Step 1. the elemental compositions of the kerogen samples were determined from elemental analysis and XPS results. The relative contents of C, O, N, and S were used to define the basic atomic composition of the kerogen molecular models. The high-resolution XPS spectra were further used to constrain the chemical states of heteroatoms. Nitrogen-containing functional groups, including pyridinic N, pyrrolic N, and quaternary N, and sulfur-containing groups, including thiophenic or aliphatic sulfur, sulfoxide, and sulfone species, were assigned according to the fitted N1s and S2p spectra.

Step 2. the carbon skeleton of the kerogen models was mainly constrained by solid-state ^{13}C NMR data. The relative proportions of aliphatic carbon, aromatic carbon, carboxyl carbon, and carbonyl carbon were determined from the integrated peak areas of different carbon types. Aromatic carbon fractions, including protonated aromatic carbon, bridged aromatic carbon, branched aromatic carbon, and oxygen-substituted aromatic carbon, were used to constrain the size, type, and connection pattern of aromatic clusters. Aliphatic carbon fractions were used to assign methyl, methylene, methine, quaternary sp^3 carbon, and oxygenated aliphatic structures.

Step 3. Oxygen-containing functional groups were assigned by combining ^{13}C NMR, FTIR, and high-resolution XPS C1s/O1s results. The relative contents of C–O, C=O, and O–C=O species were used to constrain the distribution of hydroxyl/ether groups, carbonyl groups, and carboxyl groups. FTIR spectra were used as additional evidence for identifying aromatic C=C, aliphatic C–H, hydroxyl, ether, carbonyl, and

other oxygen-containing functional groups.

Step 4. Based on these experimental constraints, initial two-dimensional kerogen molecular structures were constructed. The models were then imported into MestReNova to calculate simulated ^{13}C NMR characteristics. The simulated spectra were compared with the experimental ^{13}C NMR results, and the molecular structures were iteratively adjusted by modifying the aromatic clusters, aliphatic chains, oxygen-containing groups, and N-/S-containing functional groups. This iterative adjustment was repeated until reasonable agreement between the experimental and simulated spectral characteristics was achieved.

Step 5. After the 2D molecular structures were established, the kerogen models were further used to construct three-dimensional molecular configurations. Multiple kerogen fragments were packed using the Amorphous Cell module, followed by geometry optimization and molecular dynamics relaxation. The structures were optimized through NVT and NPT simulations to obtain stable kerogen matrices with reasonable densities. The final optimized kerogen structures were then used to construct slit-pore models for subsequent GCMC adsorption and MD diffusion simulations.

Step 6. It should be noted that the purpose of this study was not to develop a new kerogen construction method. Instead, the established kerogen reconstruction strategy was used to build experimentally constrained Longmaxi kerogen models with different maturity levels. These models were then applied to investigate the maturity-controlled competitive adsorption and diffusion mechanisms of CO_2–H_2 and CH_4–H_2 mixtures in kerogen nanopores.

Appendix B: Adsorption Formulas and Calculation Equations for Molecular Simulation

(1) Absolute and Excess Adsorption

In molecular simulation, Grand Canonical Monte Carlo (GCMC) simulations directly provide the total number of molecules within the pore space, known as absolute adsorption. However, laboratory measurements typically yield excess adsorption. These two must be converted using density relationships. Absolute Adsorption (N_{abs}). This refers to the actual total amount of adsorbate molecules contained within the adsorbent pores at a given pressure and temperature, usually expressed in mmol/g or cm^3/g. Excess Adsorption (N_{ex}) refers to the total number of molecules in the pores minus the number of molecules that would be present in the same volume according to the bulk phase density:

$$N_{ex} = N_{abs} - \rho_{gas} \cdot V_{pore} \tag{S1}$$

where ρ_{gas} is the density of the gas in the bulk phase at the simulation temperature and pressure; V_{pore} is the effective pore volume of the kerogen.

(2) Diffusion Coefficient

The diffusion coefficient describes the kinetic characteristics of gas molecules within kerogen slit pores, typically obtained through Molecular Dynamics (MD) simulations. The diffusion coefficient *D* is proportional to the rate of change of the Mean Square Displacement (MSD) over time:

$$D = \frac{1}{2n} \lim_{t\to\infty} \frac{d}{dt} \langle |r_i(t) - r_i(0)|^2 \rangle \tag{S2}$$

n: the dimensionality of the space (for 3D diffusion, *n*=3, making the coefficient 1/6). $\langle |r_i(t) - r_i(0)|^2 \rangle$ is Mean Square Displacement, which represents the average of the squared displacement of molecules at time *t* relative to their initial positions. $r_i(t)$: the position vector of the *i*-th molecule at time *t*.

(3) Radial Distribution Function (RDF)

The Radial Distribution Function $g(r)$ is an important parameter for characterizing the fluid structure and spatial distribution, used to analyze the arrangement of adsorbate molecules near the kerogen surface:

$$g(r) = \frac{V}{N^2} \langle \sum_i \sum_{j\neq 1} \delta(r - r_{ij}) \rangle = \frac{1}{\rho} \frac{dN(r)}{\rho 4\pi r^2 dr} \tag{S3}$$

where ρ is the average number density of the system. $dN(r)$: the average number of particles within the range of r to $r + dr$ from a reference particle. $4\pi r^2 dr$: the volume of the spherical shell.

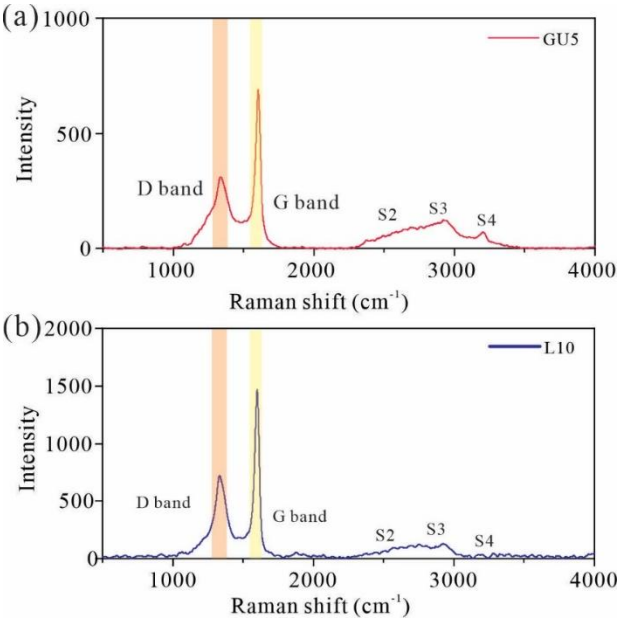


Fig. S1. Characteristics of kerogen laser Raman spectroscopy curves.

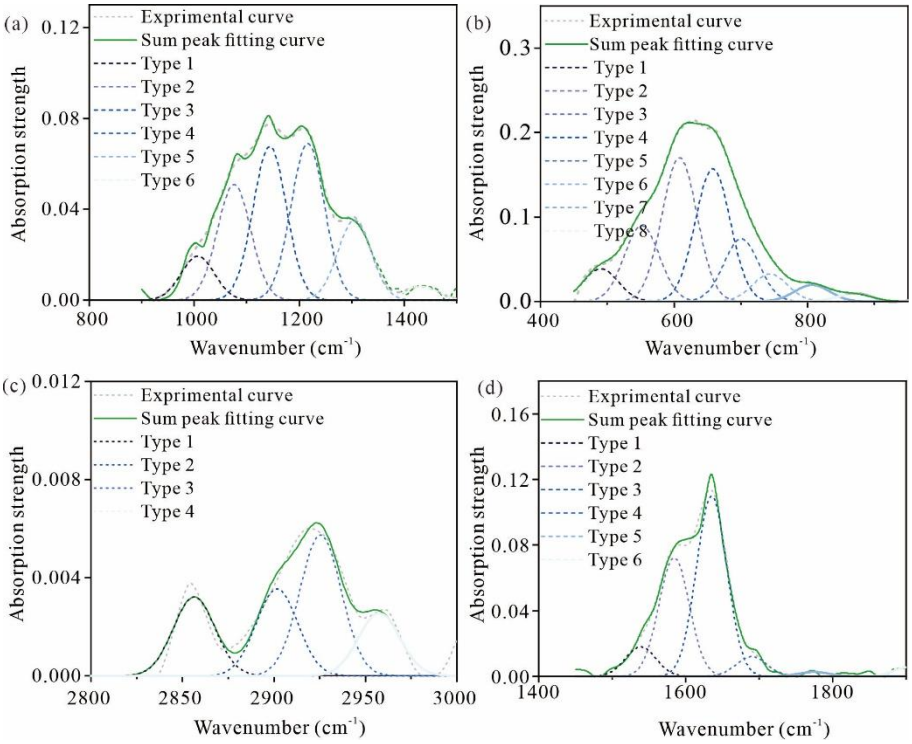


Fig. S2. Peak fitting results for kerogen in different wavelength ranges. (a) Absorbance bands of 450-950 cm^{-1}; (b) Absorbance bands of 900-1,500 cm^{-1}; (c) Absorbance bands of 1,500-1,900 cm^{-1}; (d) Absorbance bands of 2,800-3,000 cm^{-1}.

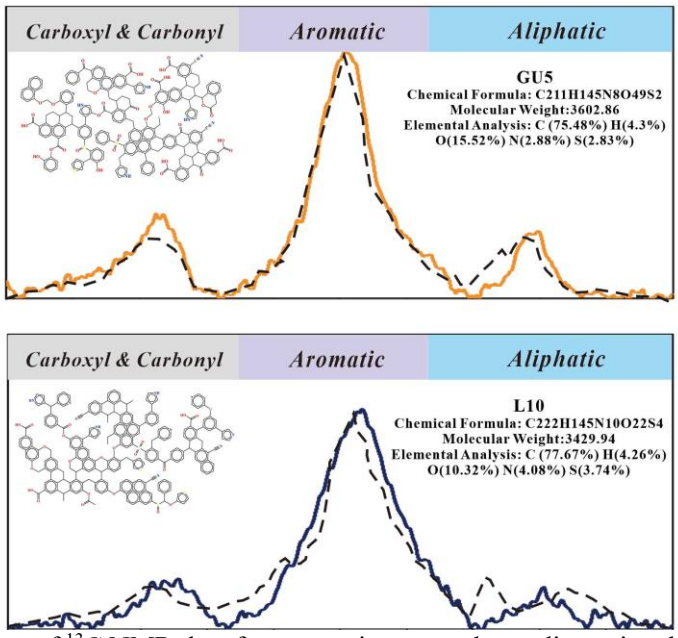


Fig. S3. Comparison of ^{13}C NMR data from experiments and two-dimensional kerogen structure estimates.

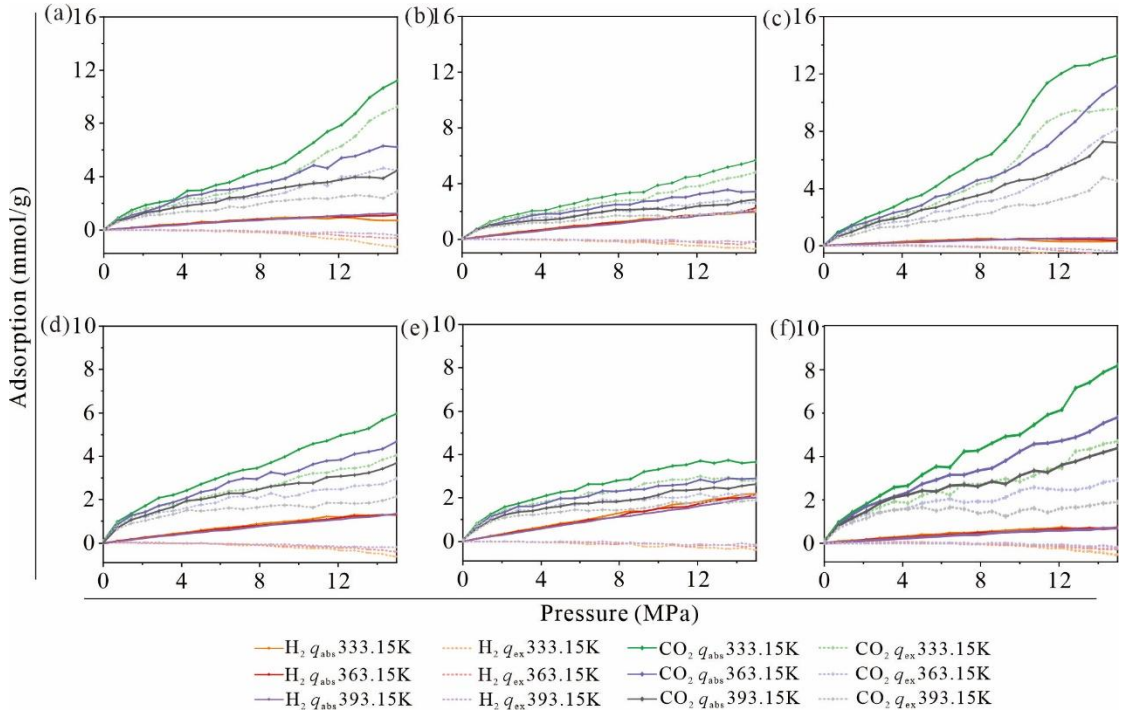


Fig. S4. Mix gas adsorption capacity of kerogen slit pores at different pressures and temperatures. (a)-(c) GU5 kerogen slit pore adsorption capacity with CO_2: H_2 at 3:1 to 1:3; (d)-(f) L10 kerogen slit pore adsorption capacity with CO_2: H_2 at 3:1 to 1:3.

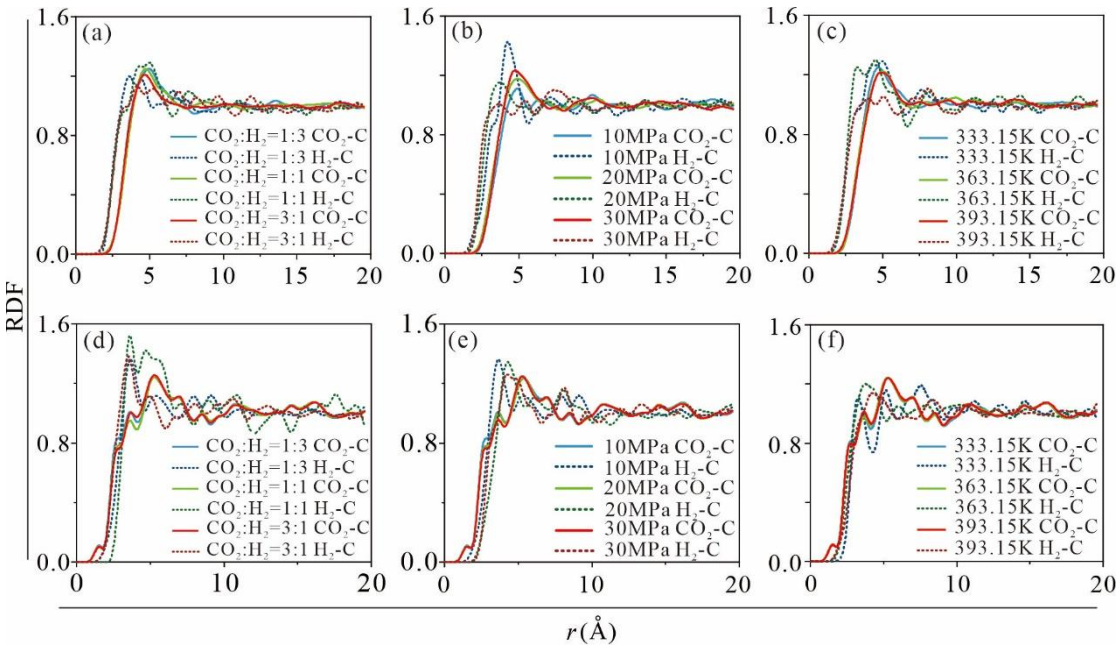


Fig. S5. RDF between gas molecules and kerogen carbon atoms in L10 under different gas compositions, pressures, and temperatures. (a) CH_4/H_2 ratio; (b) pressure-dependent CH_4-carbon RDF; (c) temperature-dependent CH_4-carbon RDF; (d) CO_2/H_2 ratio in GU5; (e) pressure-dependent CO_2-carbon RDF; (f) temperature-dependent CO_2-carbon RDF.

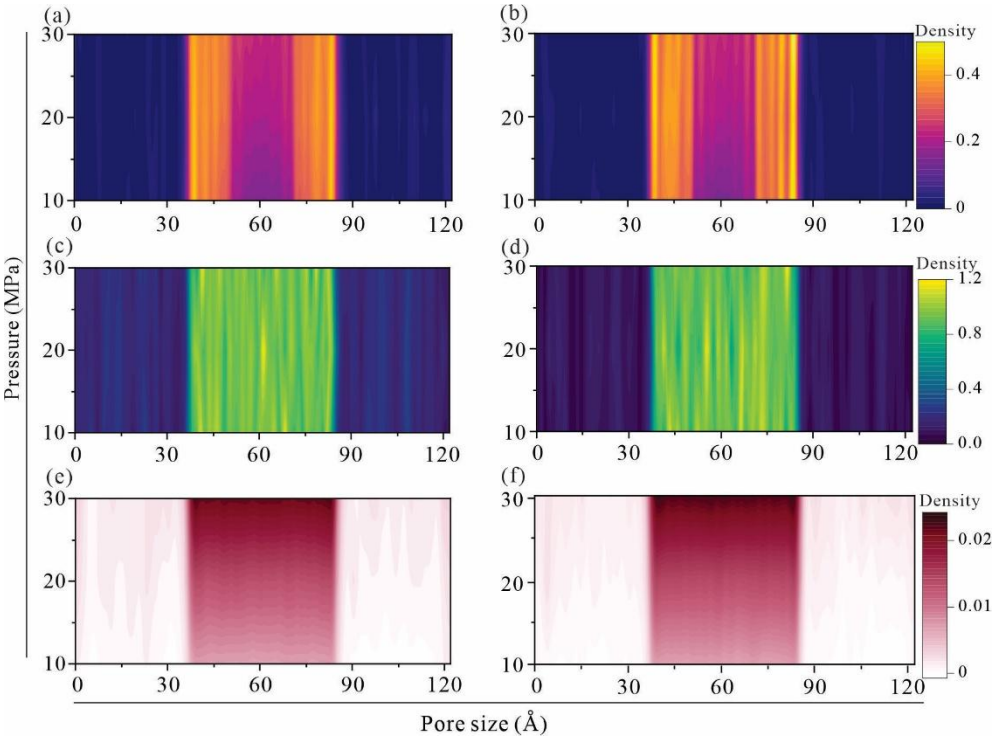


Fig. S6. Density of single-component gas under different pressure in kerogen slit pores. (a, b) CH_4 density profiles in GU5 and L10 kerogen, respectively; (c, d) CO_2 density profiles in GU5 and L10 kerogen, respectively; and (e, f) H_2 density profiles in GU5 and L10 kerogen, respectively.

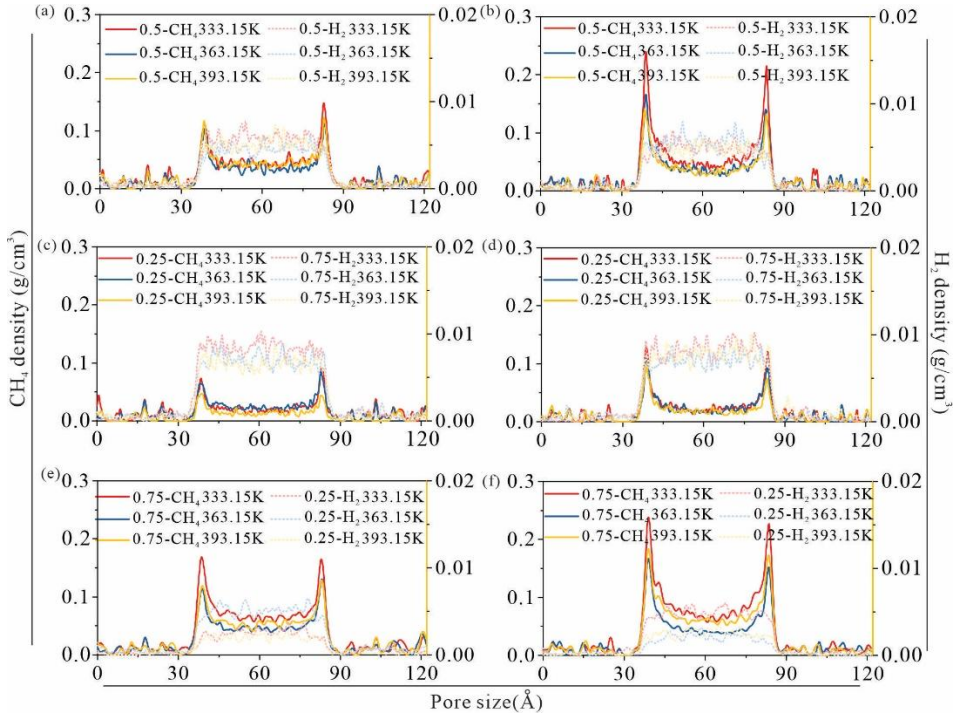


Fig. S7. Adsorption density of CH_4 with different ratios in kerogen slit pores under different temperatures. (a) G5 slit kerogen pore with 1:1; (b) L10 slit kerogen pore with 1:1; (c) G5 slit kerogen pore with 1:3; (d) L10 slit kerogen pore with 1:3; (e) G5 slit kerogen pore with 3:1; (f) L10 slit kerogen pore with 3:1.

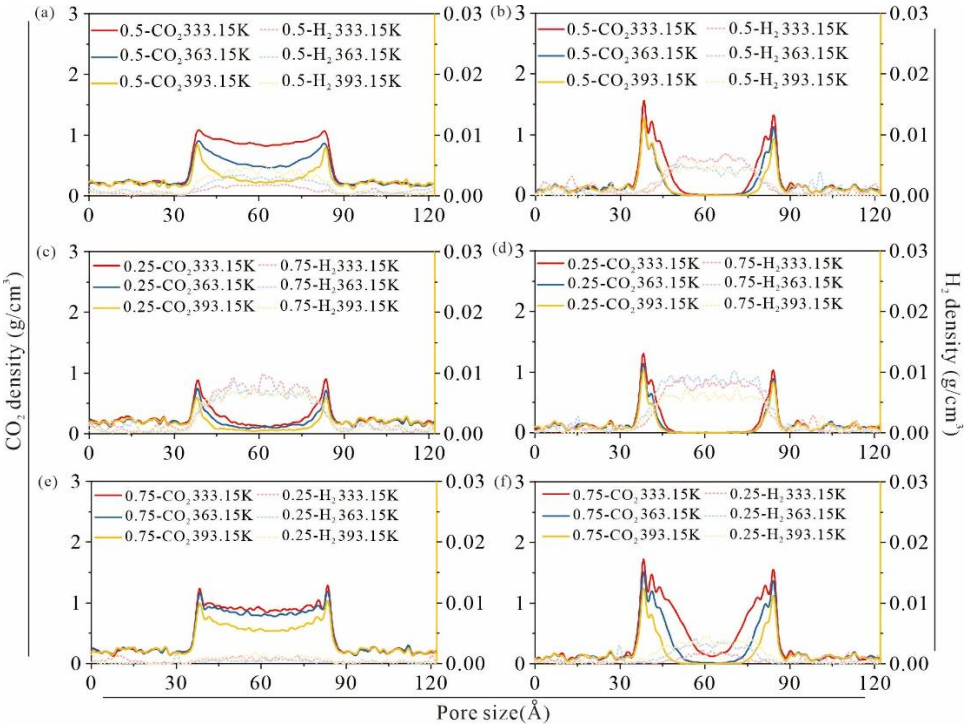


Fig. S8. Adsorption density of CO_2 and H_2 with different ratios in kerogen slit pores under different temperatures. (a) G5 slit kerogen pore with 1:1; (b) L10 slit kerogen pore with 1:1; (c) G5 slit kerogen pore with 1:3; (d) L10 slit kerogen pore with 1:3; (e) G5 slit kerogen pore with 3:1; (f) L10 slit kerogen pore with 3:1.

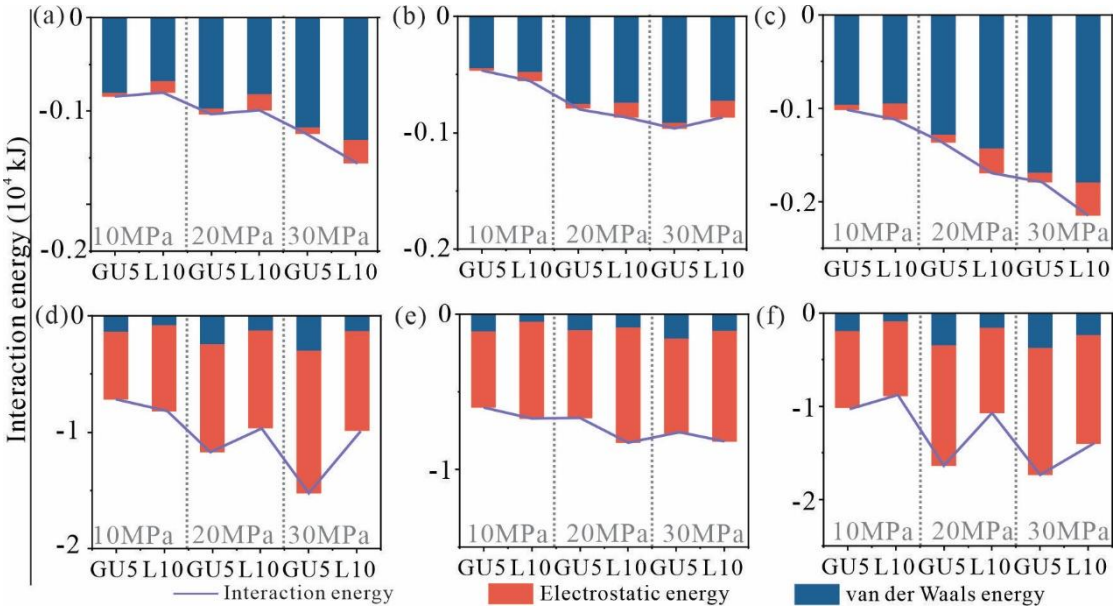


Fig. S9. Interaction energy of mixed gas in kerogen slit pores under different pressures. Interaction energies of CH_4/H_2 and CO_2/H_2 mixtures under different pressures. (a)-(c) CH_4/H_2 under different pressures with mixing ratios of 1:1, 1:3, and 3:1, respectively; (d)-(f) CO_2/H_2 under different pressures with mixing ratios of 1:1, 1:3, and 3:1, respectively.

Table S1. Comparison between the reconstructed kerogen models in this study and previously reported kerogen models.

Model	Type	Structure	H/C	O/C	Maturity	Density (g/cm^3)	Force field	Reference
Gulong shale	I	$C_{123}H_{107}N_5O_7$	0.87	0.057	1.76	1.2	CVFF	Zhang et al. (2027)
Ungerer	II-D	$C_{175}H_{102}O_9N_4S_2$	0.583	0.051	Post-mature	1.19	CVFF	Zhao et al. (2025)
Longmaxi shale	II	$C_{205}H_{158}O_{19}N_4S_4$	0.771	0.093	Immature	1.02	COMPASS II	Yang et al. (2025)
Shengli Oilfield	II	$C_{242}H_{219}O_{13}N_5S_2$	0.905	0.054	intermediate-maturity	1.01	COMPASS II	Zhang et al. (2024)
II-A kerogen	II	$C_{234}H_{365}N_3O_{25}S_3$	1.560	0.107	low-maturity	1.0	CVFF	Deng et al. (2024)
Ungerer II-C	II	$C_{242}H_{219}O_{13}N_5S_2$	0.905	0.054	Mature	1.1-1.2	PCFF	Liu et al. (2023)
Longmaxi kerogen model	I	$C_{239}H_{175}O_{27}N_5S_4$	0.732	0.113	Highly mature	1.22	COMPASS	Hou et al. (2023)
High (GU5) kerogen	I	$C_{211}H_{145}N_7O_{33}S_3$	0.687	0.156	2.89%	1.231	COMPASS	This study
Over (L10) kerogen		$C_{222}H_{145}N_{10}O_{22}S_4$	0.653	0.099	3.24%	1.248		

Table S2. Organic geochemical characteristics of different samples and sample depth information

Well	Depth (m)	S_0 (mg/g)	S_1 (mg/g)	S_2 (mg/g)	T_{max} (℃)	PG (mg/g)	GPI	OPI
GU5	3500.4	0.0041	0.7810	0.7354	320.00	0.1262	0.0027	0.5136
L10	4280.6	0.0096	0.1172	0.2658	366.00	0.0326	0.0245	0.2985

Table S3. XPS data of kerogen from Longmaxi shale.

Elements	Type	GU5	L10
C1s	Peak	278.87	284.99
	Area	16,7617.6	835,416.6
	Atomic	77.38%	82.47%
O1s	Peak	527.87	532.44
	Area	29866.57	96,497.69
	Atomic	13.79%	9.53%
N1s	Peak	400.67	401.31
	Area	10841.8	50852.7
	Atomic	5.01%	5.02%
S2p	Peak	678.87	686.95
	Area	8281.3	30270.9
	Atomic	3.82%	2.99%

Table S4. Peak assignments for FTIR spectra of kerogen samples

Wavenumber (cm^{-1})	Assignment
3,300	OH stretch intermolecular bonding
3,030	Aromatic C–H
2,950	Aliphatic CH_3
1,735; 1,690-1,720; 1,650-1,630	C=O
1,600; 1,560-1,590	
2,920; 2,850	Aliphatic CH, CH_2, and CH_3
1,600	Aromatic ring stretch
1,490	Aromatic ring stretch
1,450	CH_2 and CH_3 bend, possibility of some aromatic ring modes
1,375	-CH_3
1,300-1,110	C-O stretch and O–H bend in phenoxy structures, ethers
1,100-1,000	Aliphatic ethers, alcohols
700-900	Aromatic C–H out-of-plane bending modes

Table S5. FTIR data of kerogen from Longmaxi shale.

FITR parameters	G5	L10
I	12.566	20.661
DOC	0.747	0.935
C	0.365	0.098
A	0.056	0.043
$A(CH_2)/A(CH_3)$	2.245	1.410

Reference

Zhang Y, Liu K, Chen G, et al. Evaluating wettability of kerogen under In-Situ geological Conditions: Insight from molecular simulation of the Gulong shale Oil, Songliao Basin, NE China[J]. Fuel, 2027, 427: 139650.

Yang J, Yan Q, Deng L, et al. The non-isothermal and isothermal pyrolysis mechanism of Longmaxi type II oil shale kerogen: A ReaxFF molecular dynamics study[J]. Fuel, 2025, 380: 133169.

Zhao Y, Guan B, Zhang T, et al. CO_2 and H_2 behavior in kerogen matrix with CH4 presence: Molecular insights and implications[J]. Journal of Molecular Liquids, 2025: 128453.

Zhang Y, Jiang Y, Wei Q, et al. Insight into adsorption behaviors of shale oil in kerogen slit by molecular dynamics[J]. Fuel, 2024, 374: 132432.

Deng J, Guo S, Wan J, et al. Molecular dynamics of CH4 adsorption and diffusion characteristics through different geometric shale kerogen nanopores[J]. Chemical Engineering Journal, 2024, 500: 156784.

Liu J, Zhao Y, Yang Y, et al. Multicomponent shale oil flow in real kerogen structures via molecular dynamic simulation[J]. Energies, 2020, 13(15): 3815.

Hou D, Qiu X, Gong F, et al. Characterization of kerogen molecular structure and its effect on methane adsorption behavior: A comparative study on outcrop and core samples from Longmaxi shale[J]. Chemical Engineering Journal, 2023, 466: 143293.